Correction of MR Image Distortions Induced by Metallic Objects Using a 3D Cubic B-Spline Basis Set: Application to Stereotactic Surgical Planning

S. Skare* and J.L.R. Andersson

Metallic implants in MRI cause spin-echo (SE) images to be distorted in the slice and frequency-encoding directions. Chang and Fitzpatrick (IEEE Trans Med Imaging 1992;11:319–329) proposed a distortion correction method (termed the CF method) based on the magnitude images from two SE acquisitions that differ only in the polarity of the frequency-encoding and slice-selection gradients. In the present study we solved some problems with the CF method, primarily by modeling the field inhomogeneities as a single 3D displacement field built by 3D cubic B-splines. The 3D displacement field was applied in the actual distortion direction in the slice/frequency-encoding plane. To account for patient head motion, a 3D rigid body motion correction was also incorporated in the model. Experiments on a phantom containing an aneurysm clip showed that the knot spacing between the B-splines is a very important factor in both the final image quality and the processing speed. Depending on the knot spacing and the image volume size, the number of unknowns range from a few thousands to over 100,000, leading to processing times ranging from minutes to days. Optimal knot spacing, a means of increasing the processing speed, and other parameters are investigated and discussed.   Magn Reson Med 54:169–181, 2005. © 2005 Wiley-Liss, Inc.

Key words: MRI; distortion; metallic implants; B-splines; correction

Magnetic resonance imaging (MRI) is known for its ability to provide superior tissue contrast. Furthermore, MR images often provide better delineation of tumors compared to CT when used for the planning of radiation surgery. However, MR images suffer from geometrical distortions. Object-independent sources of distortion include main static field imperfections and gradient nonlinearities. In addition, the object (patient) induces field inhomogeneities in areas with spatially varying magnetic susceptibility (e.g., at tissue–air or tissue–bone boundaries). With conventional (non-EPI) imaging, the distortion at these boundaries is quite small—on the order of a pixel. In contrast, the susceptibility difference between metal and human tissue is much higher, and often leads to substantial geometric distortions near (nonferromagnetic) metallic implants such as aneurysm clips, stents, dental braces, etc. (1–4). The nature of the distortion depends on the degree of local field inhomogeneity and the type of pulse sequence used.

Different approaches have been used to address the geometrical distortions in spin-echo (SE) imaging. In one approach, spatial localization is achieved with the use of phase encoding along all three axes (5). The resulting image is completely free of distortions, but the scan times are on the order of an hour. In addition to long scan times, aliasing and motion artifacts occur in all three directions. Hybrid solutions with somewhat shorter scan times (thanks to readout sampling of only short segments) have also been proposed (6,7). However, phase discontinuities at the edges of the segments along the k_x direction may induce ghosting and incoherent stimulated echoes (6).

The phase evolution of a pixel is dependent on the local magnetic field and the echo time (TE). Using this information to estimate the magnetic field map has been proposed for conventional imaging (8–10) and EPI (11). By subtracting the phase from two images scanned with different TE, one can obtain a phase map that is proportional to the field inhomogeneity. Because of the 2π phase cycle, the phase map must first be unwrapped (12–16) before it is used to correct the distorted images. Multiecho approaches that circumvent the phase unwrapping process have also been proposed (17).

Another approach proposed for distortion reduction is "view angle tilting" (VAT) (18,19), whereby an extra gradient during the readout is applied in the slice-selection direction. This results in a nonorthogonal image encoding, which effectively reduces the apparent distortion at the expense of image blurring.

In an interesting postprocessing approach proposed by Chang and Fitzpatrick (20), two measurements are obtained with the same spin-echo pulse sequence, but with the signs of the readout and slice-selection gradients altered. With this method (termed the CF method), two distorted images are obtained such that the direction of distortion is reversed. From these images the distortion field can be calculated and the images can be corrected. After correction, the images can be averaged to gain signal-to-noise ratio (SNR), and hence there is a minimal penalty in terms of SNR per scan time. This method uses the reconstructed magnitude images to correct for the geometrical distortion, and relies on signal conservation. Therefore, regions with signal dropouts (e.g., due to B_1 inhomogeneities near the metallic object) cannot be rectified. Kannengiesser et al. (21), who implemented the CF method, pointed out that the technique has not been widely used up to now. We believe this is primarily because 1) each column (along the frequency-encoding direction) of the displacement field is estimated separately, which leads to a discontinuous field due to slight errors in the distortion estimates; 2) movement between the two scans is not ac-

counted for; and 3) the definition of common landmarks in the two images before correction is a complicating factor (21,22).

In a recent paper we introduced a 3D version of the CF method for distortions in EP images (23). Improvements were made to the original CF method as follows:

1. Smooth and continuous displacement fields are guaranteed by the use of smooth and continuous basis functions.
2. The number of parameters to estimate, which is very large in a 3D setting, is reduced.
3. There is no need to define common landmarks in the two images.
4. Subject movements are incorporated into the model.

In this paper we present a postprocessing method that is based on the 3D CF method, with the following important modifications:

1. We estimate the displacement field along the angle of distortion, given that there are distortions along both the slice-selection and frequency-encoding directions. The original CF method describes this angle of distortion, but only in-plane distortion corrections were presented in the original study (20).

2. The 3D field is modeled by a B-spline basis set instead of a cosine-basis set. The main difference is the local support of the B-splines vs. the global support of the cosine basis set. While the EPI distortions are of fairly low-spatial-frequency content, the distortions due to metallic objects are not. To model higher spatial frequencies, a larger basis set is required. Given the internal memory capacity of a few GBs in present-day computers, this would limit the number of basis functions that can be included for the 3D cosine set, primarily due to the storage requirements for the Hessian of the objective function. The Hessian is a matrix of size $n_{xyz} \times n_{xyz}$, i.e., the square of the total number of parameters that define the displacement field.

MATERIALS AND METHODS

Theory

A field inhomogeneity, ΔB, present in SE imaging induces geometric distortion in both the frequency and slice planes, effectively along a direction $\mathbf{v}_m$, where $\mathbf{v}_m$ depends on the slice thickness s_z, frequency-encoding voxel size s_x, excitation bandwidth ω_{exc}, and receiver bandwidth ω_{recv} [Hz/pixel] according to

$$\mathbf{v}_m = \Theta \frac{[s_x/\omega_{recv} \ 0 \ s_z/\omega_{exc}]^T}{\|[s_x/\omega_{recv} \ 0 \ s_z/\omega_{exc}]\|}$$

$$\text{where } \Theta = \begin{bmatrix} \cos\left(\xi\frac{\pi}{2}\right) & 0 & \sin\left(\xi\frac{\pi}{2}\right) \\ 0 & 1 & 0 \\ -\sin\left(\xi\frac{\pi}{2}\right) & 0 & \cos\left(\xi\frac{\pi}{2}\right) \end{bmatrix},$$

$$\xi = \begin{cases} 0 & \text{if } G_x > 0 \ \& \ G_z < 0 \\ 1 & \text{if } G_x < 0 \ \& \ G_z < 0 \\ 2 & \text{if } G_x < 0 \ \& \ G_z > 0 \\ 3 & \text{if } G_x > 0 \ \& \ G_z > 0 \end{cases}, \quad [1]$$

and $\|\cdot\|$ denotes the norm. The subscript m denotes that $\mathbf{v}_m$ is defined in the metric system, which is appropriate for determining the direction in which the anatomy moves in real-world coordinates. For practical purposes, from now on we define the distortion direction in voxel coordinates by simply dropping s_x and s_z according to

$$\mathbf{v} = \Theta \frac{[1/\omega_{recv} \ 0 \ 1/\omega_{exc}]^T}{\|[1/\omega_{recv} \ 0 \ 1/\omega_{exc}]\|} \quad [2]$$

Furthermore, the relation between magnetic field inhomogeneity and displacements, $d(\mathbf{x})$, in voxel units along $\mathbf{v}$ is defined as

$$d(\mathbf{x}) = \gamma\Delta B(\mathbf{x})\|[1/\omega_{recv} \ 0 \ 1/\omega_{exc}]\| \quad [3]$$

where $\mathbf{x} = [x, y, z]^T$. The distortions will cause compression or stretching of the image (along $\mathbf{v}$) in areas where the directional derivative of $\Delta B(\mathbf{x})$ is nonzero. Because the refocusing pulse preserves the total signal in SE imaging, this compression/stretching will give rise to an intensity (Jacobian) modulation (24). The intensity modulation in the frequency and slice directions are analogous, although the latter is due to the change in slice thickness. The resulting intensity modulation becomes

$$J(\mathbf{x}) = \left(1 + \left\langle\left[\frac{d}{dx}(d(\mathbf{x})) \ 0 \ \frac{d}{dz}(d(\mathbf{x}))\right], \mathbf{v}\right\rangle\right) = (1 + \langle\nabla d(\mathbf{x}), \mathbf{v}\rangle)$$

$$[4]$$

where $\langle\nabla d(\mathbf{x}), \mathbf{v}\rangle$ is the directional derivative of d along $\mathbf{v}$.

If we knew the $\Delta B(\mathbf{x})$ field, we could use Eqs. [2]–[4] to resample the acquired data at the points $\mathbf{x}' = \mathbf{x} + d(\mathbf{x})$ and remove both the geometric and intensity distortions using the following relation:

$$I_c(\mathbf{x}) = I_{acq}(\mathbf{x} + d(\mathbf{x})\mathbf{v})J(\mathbf{x}) \quad [5]$$

However, in reality, ΔB (and therefore d) is unknown, and hence we want to estimate d using the CF method.

Pulse Sequence Modifications for the CF Method

To obtain the appropriate input data for the CF correction method, we employ two data sets (I_+ and I_-) with opposite polarity of the slice-selection and frequency-encoding gradients, using an SE (or any other RF refocused sequence). Because the direction of the chemical shift of fat will be reversed as the gradients are negated, a leading fat saturation pulse is necessary to avoid simultaneous chemical shift and distortion differences between the two image volumes. The I_+ and I_- images are identical except for the opposite distortion directions, $+\mathbf{v}$ and $-\mathbf{v}$, and possibly also different receiver gains. Minimizing the sum-of-squares difference (SSD) between these images is what drives the correction method in the iterative search for $d(\mathbf{x})$.
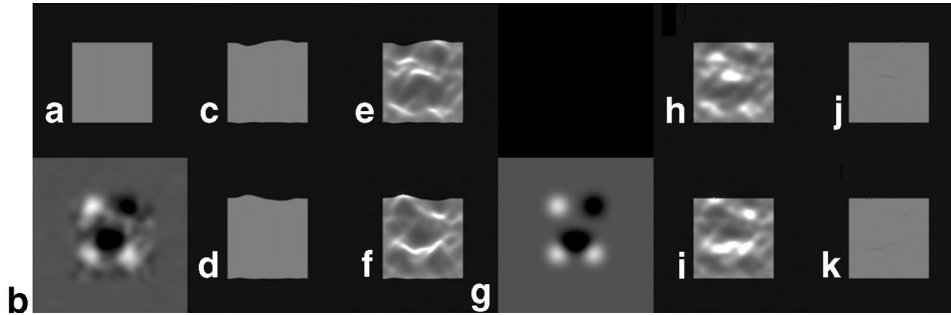
FIG. 1. Assume that we have a 2D square object (**a**) and a true 2D displacement field (**b**) that produce distortions in the vertical direction (**v** = [0 1]). Scanning with normal and reversed gradients will result in geometric distortion (**c** and **d**) and intensity modulation (**e** and **f**) of the images. **g:** The estimated displacement field $d(x,y)$, which was built of 10×10 2D B-splines (i.e., 100 unknown parameters). The scanned images (e and f) are resampled at coordinates $[x,y - d(x,y)]$ and $[x,y + d(x,y)]$ (**h** and **i**), and intensity modulated with $1 - \frac{d}{dy}(d(x,y))$ and $1 + \frac{d}{dy}(d(x,y))$ (**j** and **k**), which are very similar to the true object (a). By averaging j and k, higher SNR is obtained. The true (b) and estimated (g) fields are not the inverse of each other because the true field pushes the data to wrong locations while the estimated field is applied on the distorted images as a pulling operation.

Modeling the Displacement Field

Since the unknown $\Delta B(\mathbf{x})$ is a continuous 3D scalar field, we have in this work modeled $d(\mathbf{x})$ as such. This is in contrast to previous works, in which each column was modeled separately (20–22,25).

Estimation of a continuous 3D displacement field can be achieved by using some form of regularization and/or by building $d(\mathbf{x})$ from a basis set that is limited in spatial frequency. One advantage of a basis set is that the parameters to be estimated are the coefficients of the basis functions rather than each and every voxel in $d(\mathbf{x})$, which results in fewer parameters (by several magnitudes) to estimate.

Recently, we also used the CF method to estimate a continuous field to correct for EPI distortions. For that application we chose the cosine basis set (26) to model the 3D displacement field. The cosine set is suitable for EPI distortions, which consist of fairly low spatial frequencies. However, because of its global support the computational effort and memory storage requirements grow as the resolution of the displacement field is raised to the power of six. This poses a problem for $\Delta B(\mathbf{x})$ fields induced by metallic objects, which generate inhomogeneities of high spatial frequencies.

One way to solve this problem is to use 3D cubic B-splines (27–29). The most apparent advantage is its local support, i.e., each B-spline is nonzero only over a very limited volume, which allows the calculations to be performed in smaller pieces. A detailed definition of B-splines and how they are used in this work can be found in Appendix A. The displacement field, $d(\mathbf{x})$, which is of the same dimensions as the image data, is built up from identical 3D B-splines centered on knots placed regularly on a 3D grid. The size of each B-spline is given by the knot spacing $\mathbf{h} = [h_x, h_y, h_z]$ in voxel units. Since the support (the range in which it is nonzero) of a cubic B-spline by definition is 5 knots in each direction, each B-spline "covers" $K = (4h_x + 1) \times (4h_y + 1) \times (4h_z + 1)$ voxels. The smaller the knot spacing, the more B-splines are needed to build up $d(\mathbf{x})$, and higher spatial frequencies can be mod-

eled. After the knot spacing $\mathbf{h}$ has been defined according to the nature of the distortions and the voxel size, the modeled displacement field is given by the coefficients in the scalar field $c(\mathbf{k})$

$$d(\mathbf{x}) = \sum_{\mathbf{k} \in K} c(\mathbf{k})\beta_3(\mathbf{x}/\mathbf{h} - \mathbf{k}) \qquad [6]$$

where $\mathbf{x} = [x, y, z] \in V$, i.e. the entire image volume, $\mathbf{h}$ is the knot spacing, $\mathbf{k}$ is a shift parameter, and $c(\mathbf{k})$ is the field of B-spline coefficients. Using B-splines with equidistant knot spacing implies that the modeled function falls off to zero at the boundaries. This can potentially be an issue if there are distortions near the edges of the image volume. To circumvent this, one can simply extend the image volume with 1 or 2 knots in each direction and pad the data with zeros (30).

Estimation of the Displacement Field

Let us illustrate with a 2D example how to estimate the displacement field from the image data itself (note again that all work is actually done in 3D). Assume that we have a square object (Fig. 1a) and a magnetic field inhomogeneity, as in Fig. 1b. In this example the distortion direction, $\mathbf{v} = [0 \ 1]$, goes vertically in the image. Scanning this object twice with different signs of the readout gradient yields position shifts along $+\mathbf{v}$ or $-\mathbf{v}$ (Fig. 1c and d, respectively). Only distortions on the borders of isointensity reveal the existence of distortion when one looks at the two images. However, since the position shift also changes the apparent proton density, we get an intensity (Jacobian) modulation as well (Eq. [4], Fig. 1e and f). The two latter images correspond to the actual images we would acquire given this square object and this field. The Jacobian modulation means that we can also see the effects of distortion inside a region of isointensity.

The task now is to search for the coefficient field $c(\mathbf{k})$ that builds d using a certain knot spacing $\mathbf{h}$, which minimizes the SSD between the two scanned images (Fig. 1e

and f) after resampling (Fig. 1h and i) and intensity modulation (Fig. 1j and k). The objective function becomes

$$O(\mathbf{c}) = \sum_{\mathbf{x} \in V} [I_+(\mathbf{x} + d(\mathbf{x}, \mathbf{c})\mathbf{v}) \cdot (1 + D(d))$$

$$- I_-(\mathbf{x} - d(\mathbf{x}, \mathbf{c})\mathbf{v}) \cdot (1 - D(d))]^2 \quad [7]$$

where **c** is an unraveled vector form of $c(\mathbf{k})$, and $D(d) = \langle \nabla d(\mathbf{x}, \mathbf{c}), \mathbf{v} \rangle$ is the directional derivative of $d(\mathbf{x})$. Given that the length, *N*, of **c** may be on the order of tens of thousands, a fast search algorithm using derivatives is necessary to achieve acceptable execution times. The derivation of an expression for the first derivative of Eq. [7] is left for Appendix B.

We chose to use the variable metric (VM) method, which uses the first derivative of the objective function, as our search algorithm. The VM starts off as a gradient descent method, but in each iteration it improves an estimate of the inverse of the Hessian, which is initially set to the unity matrix, and gradually becomes more similar to the Gauss-Newton method. The advantage of the VM (over the conjugate gradient method) is that it is able to handle the different scale of the movement (see below) and distortion parameters quite gracefully.

Once a minimum of the *N*-dimensional parameter space is reached, the modeled displacement field (Fig. 1g) is an approximation to the underlying but unknown $\Delta B(\mathbf{x})$ field. The careful reader notices that the estimated displacement field (Fig. 1g) is not the scaled and approximated *inverse* of $\Delta B(\mathbf{x})$ field (Fig. 1b), as one might at first expect given that the $\Delta B(\mathbf{x})$ field generates the distortions while the displacement field corrects for the distortions. This is because $\Delta B(\mathbf{x})$ pushes the data into the wrong locations, while we use $d(\mathbf{x},\mathbf{c})$ to go into the distorted image space and pull the data into the correct locations.

For large and rapidly changing displacement fields, where the derivative of the field is larger than one, voxels with negative Jacobian will arise, leading to negative image intensities and reordering of voxels after correction, even if the true field is known (see Eq. [5]). Since these effects cannot be handled by the model, we restrict ourselves to correct the data outside this region.

Motion Between the I_+ and I_- Volumes

In a clinical setting, the two image volumes may also differ due to patient motion. Because of the high-spatial-frequency content in the $\Delta B(\mathbf{x})$ field, even subvoxel head motion will have an impact on the outcome of the correction. We therefore chose to include a 3D rigid motion model of the I_+ image to the I_- image simultaneously with the estimation of $d(\mathbf{x},\mathbf{c})$. The new objective function to minimize becomes a function of a new parameter vector **p**, given by

$$\mathbf{p} = \begin{bmatrix} \mathbf{m} \\ \mathbf{c} \end{bmatrix} \quad [8]$$

where **m** is a 6×1 vector containing the 3D rigid body motion parameters.

The objective function now becomes

$$O(\mathbf{p}) = \sum_{\mathbf{x} \in V} [I_+(\mathbf{T}(\mathbf{m})\mathbf{x} + d(\mathbf{x}, \mathbf{c})\mathbf{v}) \cdot (1 + D(d))$$

$$- I_-(\mathbf{x} - d(\mathbf{x}, \mathbf{c})\mathbf{v}) \cdot (1 - D(d))]^2$$

where, $\begin{cases} \mathbf{T}(\mathbf{m}) = \text{rigid body transformation matrix based on } \mathbf{m} \\ \mathbf{m} \quad = [x_{trans}, y_{trans}, z_{trans}, pitch, roll, yaw]^T \end{cases}$

$$[9]$$

Strictly, since $\mathbf{T}(\mathbf{m})$ is a 4×4 matrix, the 3×1 vector **x** must be extended to $[\mathbf{x}^T \quad 1]^T$ for this equation to hold.

EXPERIMENTS

The purpose of the experiments was to investigate the performance of the correction algorithm for image data on objects containing small metallic objects. Both phantom studies and a clinical scan were performed. The sign reversal of the *x*- and *z*-gradients was implemented on both an SE and an FSE sequence, for T_1-weighted and T_2-weighted imaging, respectively. However, in this study only T_1-weighted revSE images were obtained, because they are the most useful for stereotactic imaging. The excitation bandwidth, ω_{exc}, was fixed in the sequence to 860 Hz.

The phantom experiments were performed on a GE 1.5T Twinspeed system (23 mT/m, 75 T/(ms) using the whole-body gradient mode). A cylindrical phantom was filled with household gelatin, with an aneurysm clip embedded in the central part of the phantom. The clip was placed about a centimeter away from square plastic structures in the phantom (Fig. 2). A total of 80 axial contiguous 1-mm slices were scanned with FOV = 24×24 cm, resolution = 512×256 (zero-filled to 512×512), four averages, and receiver bandwidth $\omega_{recv} = \pm 15.63$ kHz/FOV = 61.05 Hz/pixel. The direction of distortion was $\mathbf{v} = \pm[0.998 \quad 0 \quad -0.071]$ ($\mathbf{v}_m = \pm[0.989 \quad 0 \quad -0.150]$). For code validation purposes, images with other resolutions, slice thicknesses, and receiver bandwidths were also acquired (data not shown).

The MR scanner used for the patient study was a GE 1.5T Echospeed system (23 mT/m, 120 T/(ms)). A stereotactic patient with a meningioma near an aneurysm clip was scanned with the revSE sequence with 18 contiguous 2-mm slices. The relevant imaging parameters were FOV = 26×26 cm (to include the fiducles), resolution = 256×256, $\omega_{recv} = 122.1$ Hz/pixel, TE/TR = 20/440 ms, and two averages. Flow compensation and fat saturation were applied. For the postprocessing, the knot spacing for the clinical case was set to $3 \times 3 \times 2$ mm.

The two image volumes of the phantom, each of which originally consisted of 21 million voxels, were cropped in the *xy*-plane to exclude irrelevant embedded oil bottles in the phantom far from the metallic clip. The number of voxels in each of the two cropped image volumes, centered on the clip, was reduced by one order of magnitude to $151 \times 174 \times 80$, corresponding to a volume size of $70.8 \times 81.6 \times 80$ mm³. To investigate convergence speeds and optimal spatial resolution of $d(\mathbf{x})$, we applied our CF cor-

FIG. 2. The phantom used in this work was filled with a water gel solution. An aneurysm clip was embedded in the gel near plastic structures.
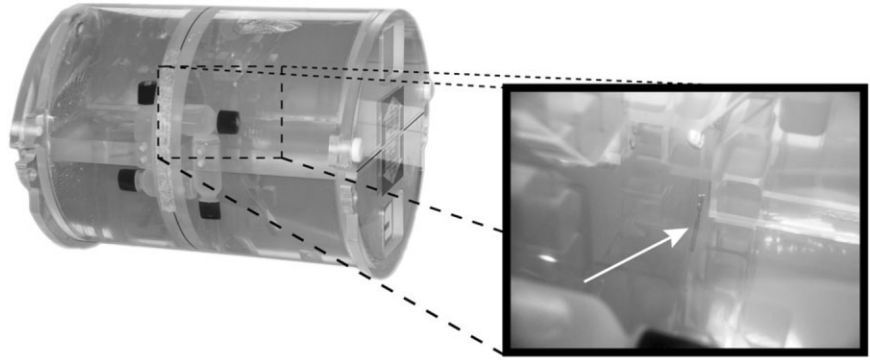
rection algorithm to the cropped image data using different knot spacings. These spacings ranged from $10 \times 10 \times 10$ mm to $2 \times 2 \times 2$ mm, which is equivalent to ~400 to ~60,000 parameters. For all runs, the termination criterion was fixed to 30 iterations. The current estimate of **c** was stored for each iteration so that the results with different iteration lengths could be compared.

Due to current implementation with *integer* knot spacing, the image volume size was padded with zeros to maintain full support for the last B-spline in each direction. Since the outermost B-splines (and therefore also $d(\mathbf{x})$) fall off to zero at the volume edges, no distortions can be modeled at the border of the volume. To circumvent this, an extra knot was added on each of the six sides of the volume.

The most time-consuming operation in the calculation of $O(\mathbf{p})$ (Eq. [9]) is the resampling of the image volume based on the current estimate of **p**. One way to reduce the calculation time of $O(\mathbf{p})$, during the estimation process only, is to reduce the image resolution. To test this, we also performed runs in which the voxel size of the image volumes was increased by a factor of 2 in each direction on phantom data. The subsampling was done by averaging rather than interpolating the voxels to gain SNR. While these low(er)-resolution image volumes were used to estimate $d(\mathbf{x})$, the estimated displacement field was eventually applied to the original image data. Cubic B-spline interpolation (which is not to be confused with the cubic B-splines forming $d(\mathbf{x})$) was used for image resampling during the iteration process.

All routines were written in C with a Matlab interface and run on a Linux 2.67 GHz CPU with 4 GB of RAM.

RESULTS

In Fig. 3, axial (a–c) and reformatted sagittal views (d–f) of the phantom are shown. The white dashed lines show the location of the other image plane. Figure 3a and d, and b and e represent the uncorrected I_+ and I_- image volumes, respectively. The corresponding difference images, $I_\Delta = |I_+ - I_-|$, are presented in Fig. 3c and f. The axial slice (Fig. 3a–c) is located a few millimeters from the aneurysm clip, just outside the core area where the pixels shifts are so large that there is no proper object information in either image. In Fig. 3d–f one can anticipate the distortion direc-
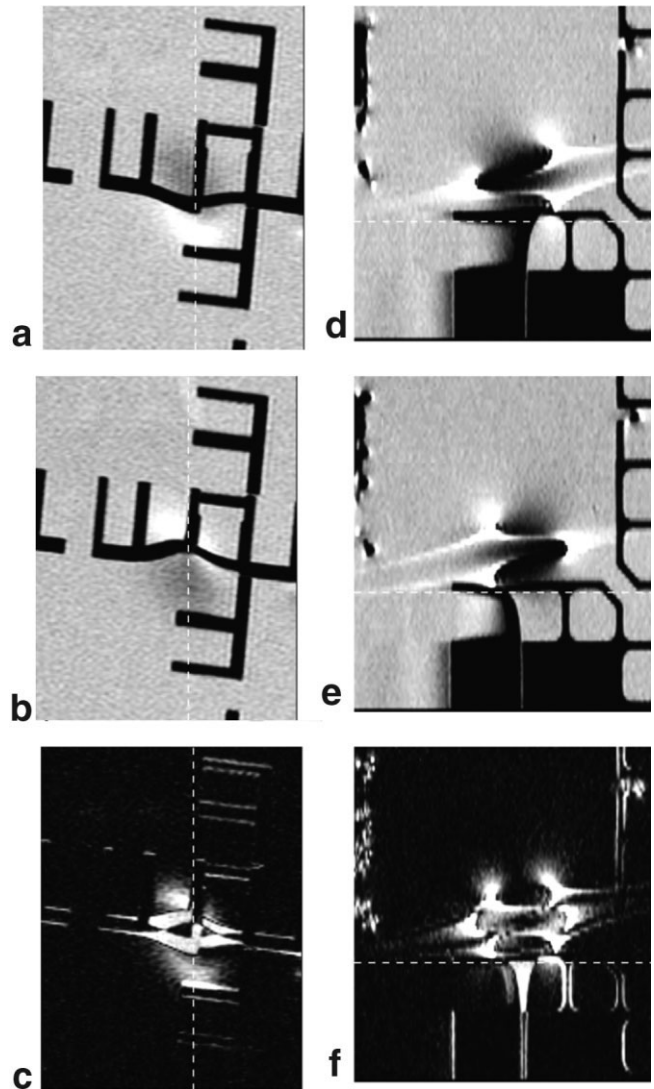

FIG. 3. Phantom data. Axial images (**a**) I_+ and (**b**) I_-, scanned with normal and reversed gradients, respectively. **d** and **e:** A sagittal cross section of the image volumes corresponding to the dashed vertical lines in a and b, and vice-versa. **c** and **f:** The absolute difference image $I_\Delta = |I_+ - I_-|$
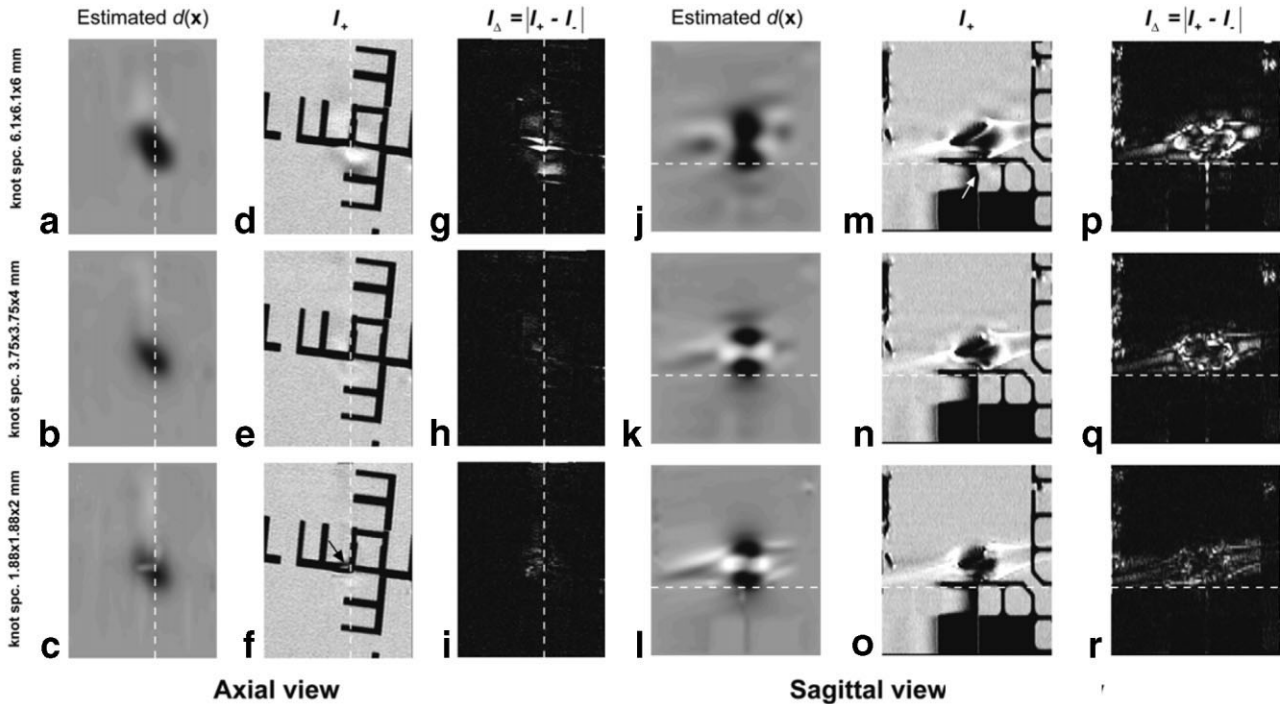
FIG. 4. Corrected data. The data in **a–i** and **j–r** correspond to the slice locations in Fig. 3. In this figure the estimated $d(\mathbf{x})$, the corrected I_+, and the I_Δ images are shown for three different resolutions of the displacement field. With ~6 mm knot spacing (top row) the field has insufficient resolution to adequately correct for the distortions. This can be appreciated by the residual intensity modulation in d and the remaining I_Δ intensity in g. By comparing m and n, it is also evident that there are remaining distortions in the middle below the dashed line (white arrow). At ~4 mm knot spacing (mid row), the best results were obtained as shown by the straight and homogeneous shapes of the phantom in e and n, as well as very low I_Δ intensity in **i** and **r** (below the dashed line). It is not obvious that the results improve by going to smaller knot spacing (i.e., 2 mm). Note, for example, the artifactual structure indicated by the black arrow in f. The same grayscale levels as in Fig. 3 have been used.

tion $\mathbf{v}_m$ by looking at the angle of the white stripes originating from the location of the clip.

The performance of the correction of the image volumes in Fig. 3 was primarily dependent on the choice of knot spacing. For knot spacings over about $5 \times 5 \times 5$ mm, the estimated displacement field had a too-low spatial frequency content to adequately model the distortions close to the clip. This is illustrated in Fig. 4, in which columns 1–3 (axial view) and 4–6 (sagittal view) display the estimated field, the corrected I_+ image, and the difference image after correction, respectively. The difference in $d(\mathbf{x})$ for knot spacings of $6.1 \times 6.1 \times 6$ mm (Fig. 4j) and $4.2 \times 4.2 \times 4$ mm (Fig. 4k) is obvious. The corresponding corrected I_+ and I_Δ image reveals residual distortions for the larger knot spacing, most notably in the area below the clip (Fig. 4d, g, m, and p). However, for 3–4-mm knot spacing, which was found to be optimal for this clip and phantom, the correction algorithm performed quite well. In both the axial and sagittal views the rectangular plastic objects in the I_+ image appear straight and the I_Δ image shows little residual mismatch. Knot spacing smaller than 3 mm did not improve the performance. At the smallest knot spacing tested in this work (~$2 \times 2 \times 2$ mm), excessive warps occurred in regions with or near low signal intensity, which can be appreciated in the center of the image of the axial I_+ (black arrow, Fig. 4f). This is reasonable, because for small knot spacings each B-spline supports a smaller

volume, which makes its coefficient less accurate due to noise.

The quadratic relationship between the processing time and the size of the coefficient field $c(\mathbf{k})$ is demonstrated in Fig. 5a for various knot spacings ranging from 2 to 10 mm. For our image volume size, the size of $c(\mathbf{k})$ became $11 \times 13 \times 13$, $18 \times 21 \times 19$, and $37 \times 43 \times 39$ for $6.1 \times 6.1 \times 6$, $4.2 \times 4.2 \times 4$, and $1.88 \times 1.88 \times 2$ mm knot spacing, respectively, yielding processing times of about 30 min, 45 min, and 18½ hr, respectively.

The goal of subsampling the image volumes during the correction is to increase processing speed without (at best) affecting the estimate of $d(\mathbf{x})$ as the metric knot spacing is kept constant. In this case, with a subsampling of $2 \times 2 \times 2$, there is an eightfold decrease in the number of voxels. The estimated $d(\mathbf{x})$ is rescaled and finally applied on the original image data. In Fig. 5b, the sum-of-squares difference (SSD) of the image volumes with the current estimate of $d(\mathbf{x})$ is plotted against the processing time, with and without subsampling of the image volumes during the iteration. The SSD is calculated from the original data in both cases in order to achieve a fair comparison (i.e., there are no differences in partial volume effects between the two curves of Fig. 5b, but only because of the accuracy of the current $d(\mathbf{x})$). For both curves the metric knot spacing was $3.75 \times 3.75 \times 4$ mm. As expected, subsampling made the SSD decrease faster, though not quite as fast as in
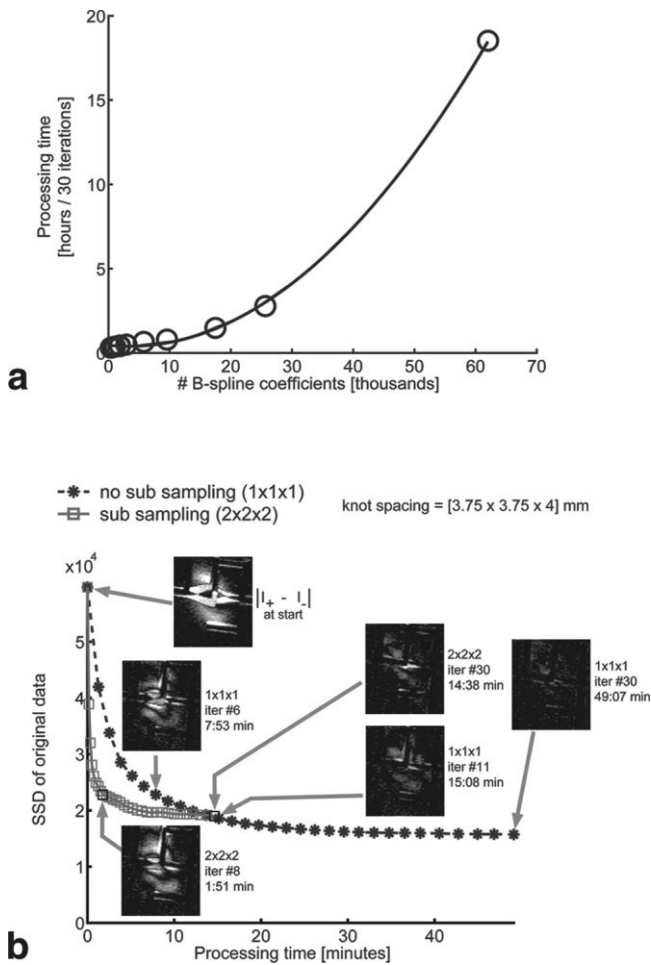
FIG. 5. **a:** The quadratic dependence between processing time and the total number of B-spline coefficients is presented. The rightmost data point corresponds to [1.88 × 1.88 × 2] mm knot spacing, which was found to be suboptimal with respect to both processing time and correction performance (Fig. 4). **b:** The SSD of the original image data is plotted vs. the processing time for the "optimal" [3.75 × 3.75 × 4] mm knot spacing. For the solid curve (□), a 2 × 2 × 2-fold reduction in the I_+ and I_- image volume sizes was obtained by nearest-neighbor averaging before the correction started to increase the processing speed. For the dashed curve (*), no subsampling was performed, and hence the initial convergence is slower. However, after 10–15 min the SSD of the solid curve stops decreasing, while the I_Δ images reveal that the objective function has not reached its asymptote. After 49 min (30 iterations without subsampling), the estimate of $d(\mathbf{x})$ does not change any further.

theory. However, after the larger mismatches are corrected, the residual distortions can only be addressed without subsampling. This can be elucidated by comparing the six I_Δ images in Fig. 5b referring to different iteration steps (e.g., after <2 min the same degree of distortion correction is achieved using subsampling as was achieved after nearly 8 min without). After 15 min, the curves cross. For the presented slice, slightly better performance was obtained without subsampling. Still, there are improvements to be made on the displacement field at this point. After 30 iterations without subsampling, I_Δ reached its final minimum intensity for the given knot spacing. A test with 100

iterations confirmed that there are no apparent improvements in I_Δ over 30 iterations (data not shown).

In Fig. 6 two axial cross sections through the meningioma of the patient are shown. Panels a–d are located 0.8 mm below panels e–h. Panels a and e, and b and f show the uncorrected I_+ and I_- images, respectively. The corresponding corrected I_+ images are presented in c and g. In panels d and h the average of the corrected I_+ and I_- image is depicted, which ideally should be identical to c and g except for the higher SNR. Any residual mismatch between the corrected images should come out as blurring in panels d and h, which we find not to be the case. In a comparison of a and b, the shape of the tumor differs considerably, which is likely to impair proper surgical planning. Furthermore, the vessel (white arrow, Fig. 6h) running posterior to the tumor is visible but distorted in a and b, and is hard to distinguish in panel e. After correction the vessel is correctly depicted in both d and h, as can be judged by following the vessel across the slices, as well as by looking at the I_Δ images (not shown), which reveal virtually no residual mismatch.

DISCUSSION

The method proposed in this work is more robust to noise because it works with a continuous 3D distortion field instead of about $n_y \times n_z$ individual 1D fields. The latter may introduce signal discontinuities in the corrected image (see, e.g., Fig. 4 in Ref. 23). Furthermore, our 3D approach corrects for distortion in the actual distortion direction (**v**), which is important because the through-plane distortion is seldom negligible. For example, in a typical clinical setting, voxel excitation/receiver bandwidths of 860/125 Hz, slice thicknesses of ~4 mm, and frequency-encoding pixel sizes of ~1 mm are common, and result in distortion angles on the order of 30°. The angle increases for higher receiver bandwidths and thicker slices. To correct the data along **v**, preferably thin slices with little cross-talk are desired to obtain continuous data in the slice direction.

The use of basis functions for the displacement field, together with a 3D rigid body motion correction included in the model, eliminates the need to define anatomical landmarks or edges, and at the same time allows scanning of patients without the use of stereotactic frames or other types of fixation devices. Since head movements are 3D, including rotations, 1D correction approaches will also have problems defining common landmarks due to inter-volume motion.

Despite the use of basis functions, the number of parameters is several thousand in a 3D setting. Since a single 3D field is to be estimated, the problem is not really suitable for parallel processing either. Consequently, code optimization and the use of fast search algorithms utilizing the derivatives of the objective function are required to achieve convergence within reasonable times. The use of a B-spline instead of a cosine basis set was necessary because the latter would have required from several GB up to more than one TB of RAM for similar resolutions of the displacement fields used in this work, not to mention massive computation time. This is because the cosine set has *global* support, implying that each cosine term to be
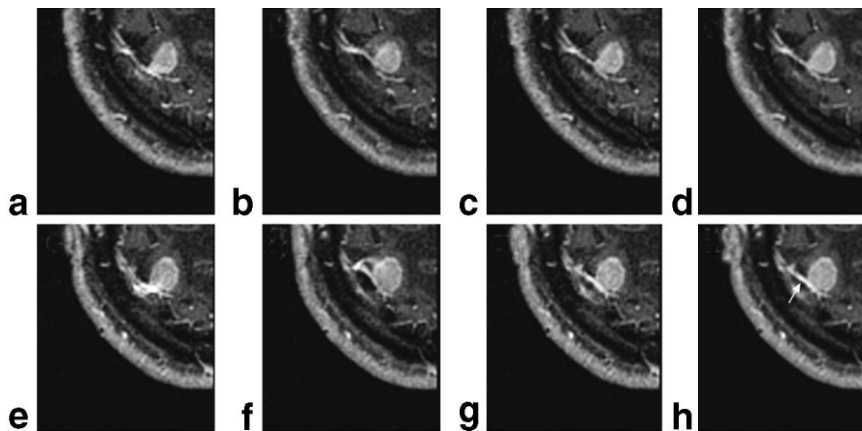
FIG. 6. Patient data. An axial slice near the metallic clip, showing the distortion near the meningioma. Panels **a–d** are located 0.8 mm below panels **e–h**. Panels a and e, and b and f show the uncorrected I_+ and I_- images, respectively. c and g: The corresponding I_+ images after correction. d and h: The average of the corrected I_+ and I_- images is given, which clearly has higher SNR compared to c and g, without introducing significant blurring. A knot spacing of $3 \times 3 \times 2$ mm was used. h: The white arrow points to a vein that is visible after distortion correction.

determined depends on the entire image volume. Also, a change in a single cosine term affects all other terms. On the other hand, the B-spline set has *local* support, meaning that each cubic B-spline covers only a subvolume (($4 \times$ knotspacing $+ 1)^3$ voxels). Even though the displacement field covers the entire volume, each B-spline does not, which makes it feasible to work with at clinically relevant resolutions for SE imaging.

We primarily worked on phantom data of the same size and computational burden as for typical clinical scans (151×174 with 80 slices $\approx 256 \times 256$ with 32 slices) and managed to get promising results within less than an hour. We consider this duration to be the upper limit for stereotactic planning applications. Longer processing times may prolong the time the patient has to wear the uncomfortable stereotactic frame. For other types of patients who do not require the stereotactic frame, several hours of processing time may be acceptable.

The subsampling technique presented in Fig. 5b shows that a "multi-image resolution" approach could reduce the processing time to some extent. By first performing a few iterations with subsampled image data and then continuing with the full-resolution image data, one could reduce the processing time by 10–15%. This is not a considerable reduction, but for other scenarios in which larger knot spacings are optimal, the subsampling technique would be more beneficial because the smoothness of the displacement field is then higher in relation to the subsampled image data used in the process.

We also experimented with increasing the processing speed by using a multi-resolution approach for the displacement field, as was previously proposed for B-splines for spatial normalization (30,31) (data not shown). One starts the process with a higher knot spacing to obtain a coarse estimate of the field. Then the displacement field is rebuilt by B-splines with smaller knot spacing to also model higher frequencies in the field. Although this transition of B-spline resolution can be made exact (30,32), and has been reported to be effective (33), we found the benefit to be limited on the phantom data. Considering the different appearances of the $d(\mathbf{x})$ field in Fig. 4j–l, the change in knot spacing implies that a lot of rebuilding rather than refining of the field has occurred in the core area of the clip, where the distortions are not correctable anyway.

A further approach to reduce the number of knots could be to use variable knot spacing, i.e., different resolutions of the field across the (full) volume. Denser knot spacing could be defined either manually or automatically for areas in which the original mismatch between I_+ and I_- is higher. Possibly, the knot spacing could also be dynamically changed during the iteration process. However, this would require continuous recalculations of the B-splines, which would counteract the goal of short computation times.

For the phantom data used in this work, excessive warps occurred with knot spacings of $2 \times 2 \times 2$ mm. To prevent this, we tried to use the second directional derivative of the field as a regularization term. Preliminary results show that this did not have a significant impact on the residual mismatch of the phantom images. However, this may change with other objects and SNR levels.

Since T_1-weighted images are often scanned with two averages to achieve a clinically acceptable SNR, there is a minimal SNR per scan time penalty associated with the use of this method. In fact, we expect that our averaging of two motion-corrected magnitude image volumes will perform better than standard complex averaging in k-space because interacquisition phase inconsistencies and blurring due to potential motion are affected only in the latter.

CONCLUSIONS

The reversed-gradient CF method can be used to correct distortions from the magnitude images themselves, without the need to scan, calculate, and unwrap a separate phase map. We have shown that by modeling the distortion field as a continuous 3D field built from cubic B-splines, good distortion correction is obtained without introducing discontinuities in the corrected images. A 3D rigid body correction between the two scanned image volumes was also included in the process to allow correction for patients without stereotactic frames. We scanned only one clinical case involving a metallic clip near a meningioma. Other clinical cases, such as stents in the spine, remain to be explored.

APPENDIX A
B-Splines

A cubic (or third-order) 1D B-spline (B as in "basic") is defined as follows (30,34):
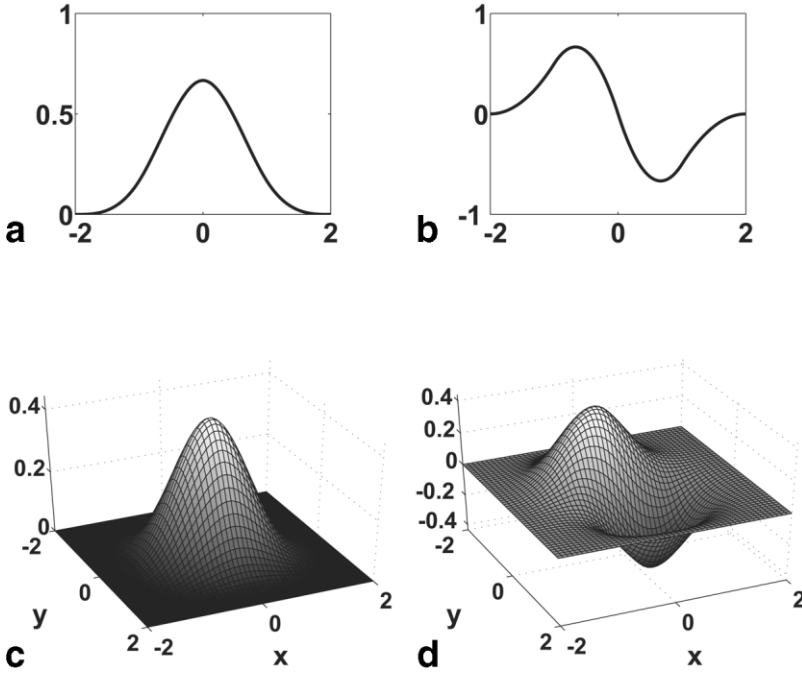
FIG. A1. Illustration of (**a**) 1D and (**c**) 2D cubic B-splines, β_3. **b** and **d:** The first derivative for the 1D and 2D case, respectively. In **d**, the arbitrary chosen distortion direction $\mathbf{v} = [0.45\ 0.89]^T$ can be appreciated. In this work, 3D cubic B-splines and its first directional derivative along the distortion direction, **v**, were used.

$$\beta_{3,x}(x) = \begin{cases} \frac{2}{3} - (1 - |x|/2)x^2 & ; 0 < |x| \leq 1 \\ (2 - |x|)^3/6 & ; 1 < |x| \leq 2 \\ 0 & ; |x| > 2 \end{cases} \quad [\text{A1}]$$

and is depicted in Fig. A1a. The B-spline is nonzero only over the $[-2,2]$ interval, in which each integer value is referred to as a "knot." Hence a cubic B-spline always covers (is nonzero over) five knots. The first derivative of the B-spline is (Fig. A1b):

$$\beta'_{3,x}(x) = \begin{cases} \frac{3}{2}\, sign(x)x^2 - 2x & ; 0 < |x| \leq 1 \\ -\frac{sign(x)}{2}(2 - |x|)^2 & ; 1 < |x| < 2 \\ 0 & ; |x| \geq 2 \end{cases} \quad [\text{A2}]$$

In Eqs. [A1] and [A2], the knot spacing is unity and thus was omitted. A 3D cubic B-spline with knot spacings h_x, h_y and h_z is obtained from three 1D B-splines in x, y, and z using the Kronecker tensor product:

$$\beta_3 = \beta_3(x,y,z) = \beta_{3,z}(z/h_z \otimes \beta_{3,y}(y/h_y) \otimes \beta_{3,x}(x/h_x) \quad [\text{A3}]$$

A 2D version is shown in Fig. A1c. Numerically, the three 1D B-splines vectors $z\beta_{3,x}$, $\beta_{3,y}$, and $\beta_{3,z}$ are column vectors of size $n_x \times 1$, $n_y \times 1$, $n_z \times 1$, and the Kronecker tensor products yield a vector of size $n_x n_y n_z \times 1$, which is an unraveled vector representation of the 3D B-spline.

A general spline curve S (e.g., a displacement curve $d(x)$) uses B-splines as building blocks, each shifted by one knot. The coefficients (or weighting) of the B-splines and the knot spacing determines the final shape of the curve. In theory, the knot spacing does not need to be equidistant.

Non-equidistant knot spacing can provide an efficient way to represent curves that are irregular in one part (dense knot spacing required) and smooth in another part (sparser knot spacing suitable) of the curve. However, for our purposes (i.e., we want to build up a 3D spline curve (the displacement field) without any a priori knowledge of the true underlying $\Delta B(\mathbf{x})$ field), the knot spacing was chosen to be equidistant in each of the three dimensions. The use of variable knot spacing would also be more time-consuming because of the variable size of the B-splines.

An example of a 1D spline curve is illustrated in Fig. A2, where the spline curve consists of 11 B-splines with coefficient vector $\mathbf{c} = [0\ 1\ 1\ 1\ 1\ 0\ -0.2\ 0\ 0.3\ 0\ 0]$ and $11+4$ knots in total. Figure A2a shows each individual B-spline, weighted with the corresponding element in $\mathbf{c}$, and the sum of these (Fig. A2c) is written as

$$S(x) = \sum_{k \in Z} \mathbf{c}(k)\beta_3(x/h_x - k) \quad [\text{A4}]$$

The first derivative of S is simply obtained by weighting $\beta'_3(x/h_x)$ with $\mathbf{c}$ (Fig. A2b), yielding (Fig. A2d)

$$S'(x) = \sum_{k \in Z} \mathbf{c}(k)\beta'_3(x/h_x - k) \quad [\text{A5}]$$

The expression for the 3D displacement field, $d(\mathbf{x})$, becomes

$$d(\mathbf{x}, \mathbf{c}) = d(x, y, z) = \sum_{(k_x,k_y,k_z) \in K} c_{k_x,k_y,k_z}\{\beta_3(x/h_x - k_x) \\ \times \beta_3(y/h_y - k_y)\beta_3(z/h_z - k_z)\} \quad [\text{A6}]$$

and can be rapidly calculated since the 3D β_3 (due to fixed knot spacing) only has to be calculated once and then
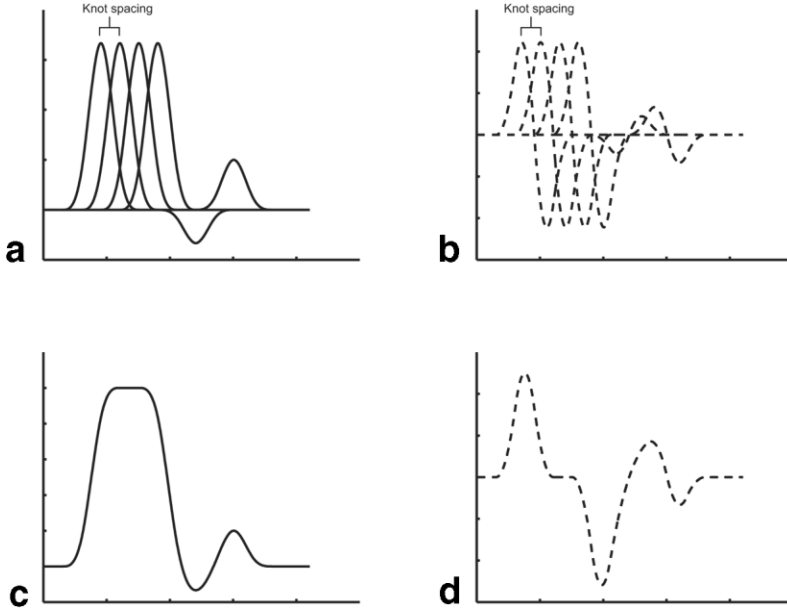
FIG. A2. A 1D example of how (**a**) cubic B-splines and (**b**) their first derivatives build (**c**) the displacement field and (**d**) its first derivative (used for intensity modulation). A set of 11 1D (a) cubic B-splines and (b) first derivatives of different amplitudes defined by coefficient vector $\mathbf{c} = [0\ 1\ 1\ 1\ 1\ 0\ -0.2\ 0\ 0.3\ 0\ 0]$ is shown. The splines are shifted relative to each other by one "knot" that generates curves c and d. In 3D, the vector c is a 3D coefficient field.

applied to different parts of the image volume. After the I_+ and I_- images are resampled using $d(\mathbf{x})$, the data are intensity modulated, which involves the current estimate of the directional derivative of $d(\mathbf{x})$:

$$D_{\mathbf{v}}(d(\mathbf{x})) = \langle \nabla d(\mathbf{x}), \mathbf{v} \rangle$$

where

$$\nabla d(\mathbf{x}) = \begin{bmatrix} \sum_{(k_x,k_y,k_z)\in K} c_{k_x,k_y,k_z}(\beta_3'(x/h_x - k_x)\beta_3(y/h_y - k_y)\beta_3(z/h_z - k_z)) \\ \sum_{(k_x,k_y,k_z)\in K} c_{k_x,k_y,k_z}(\beta_3(x/h_x - k_x)\beta_3'(y/h_y - k_y)\beta_3(z/h_z - k_z)) \\ \sum_{(k_x,k_y,k_z)\in K} c_{k_x,k_y,k_z}(\beta_3(x/h_x - k_x)\beta_3(y/h_y - k_y)\beta_3'(z/h_z - k_z)) \end{bmatrix} \quad [\text{A7}]$$

For a fast implementation of Eq. [A7], the directional derivative of the 3D B-spline is first calculated once

$$D_{\mathbf{v}}(\boldsymbol{\beta}_3) = \langle \nabla \boldsymbol{\beta}_3, \mathbf{v} \rangle = \begin{bmatrix} (\boldsymbol{\beta}_{3,z} \otimes \boldsymbol{\beta}_{3,y} \otimes \boldsymbol{\beta}_{3,x}')^T \\ (\boldsymbol{\beta}_{3,z} \otimes \boldsymbol{\beta}_{3,y}' \otimes \boldsymbol{\beta}_{3,x})^T \\ (\boldsymbol{\beta}_{3,z}' \otimes \boldsymbol{\beta}_{3,y} \otimes \boldsymbol{\beta}_{3,x})^T \end{bmatrix}^T \mathbf{v} \quad [\text{A8}]$$

and then

$$D_{\mathbf{v}}(d(\mathbf{x})) = \sum_{(k_x,k_y,k_z)\in K} c_{k_x,k_y,k_z}(D_{\mathbf{v}}(\boldsymbol{\beta}_3)) \quad [\text{A9}]$$

A 2D version of $D_{\mathbf{v}}(\boldsymbol{\beta}_3)$ with $\mathbf{v} = [0.45 \quad 0.89]^T$ is shown in Fig. A1d.

APPENDIX B
The Objective Function and its First Derivative

The objective function used in work is

$$O(\mathbf{p}) = \sum_{\mathbf{x} \in V} [I_+(\mathbf{T}(\mathbf{m})\mathbf{x} + d(\mathbf{x}, \mathbf{c})\mathbf{v})(1 + D_{\mathbf{v}}(d(\mathbf{x}, \mathbf{c})))$$

$$- I_-(\mathbf{x} - d(\mathbf{x}, \mathbf{c})\mathbf{v})(1 - D_{\mathbf{v}}(d(\mathbf{x}, \mathbf{c})))]^2 \quad [\text{B1}]$$

where $\mathbf{x} = [x \quad y \quad z \quad 1]^T$, $\mathbf{m} = [x_{trans},\ y_{trans},\ z_{trans},\ pitch,\ roll,\ yaw]^T$ are the six rigid body motion parameters to be estimated, $\mathbf{T}(\mathbf{m})$ is the corresponding transformation matrix, $\mathbf{c}$ is the coefficient vector, $\mathbf{p} = [\mathbf{m}^T \quad \mathbf{c}^T]^T$ is the full parameter vector, $\mathbf{v} = [1/\omega_{recv} \quad 0 \quad 1/\omega_{exc}]^T/\|[1/\omega_{recv} \quad 0 \quad 1/\omega_{exc}]\|$ is the distortion direction, and $D_{\mathbf{v}}(d) = \langle \nabla d(\mathbf{x}, \mathbf{c}), \mathbf{v} \rangle$ is the first directional derivative of d

Equivalently, we could express Eq. [B1] in vector form as

$$O(\mathbf{p}) = (\mathbf{f}_+ - \mathbf{f}_-)^T(\mathbf{f}_+ - \mathbf{f}_-) \quad [\text{B2}]$$

where

$$\begin{cases} \mathbf{f}_+ = \mathbf{I}_+ \odot \mathbf{J}_+ = [I_+(\mathbf{T}(\mathbf{m})\mathbf{x} + d(\mathbf{x}, \mathbf{c})\mathbf{v})] \odot [1 + D_\mathbf{v}(d(\mathbf{x}, \mathbf{c}))] \\ \mathbf{f}_- = \mathbf{I}_- \odot \mathbf{J}_- = [I_-(\mathbf{x} - d(\mathbf{x}, \mathbf{c})\mathbf{v})] \odot [1 - D_\mathbf{v}(d(\mathbf{x}, \mathbf{c}))] \end{cases}$$

and where $\odot$ denotes element-wise multiplication.

Derivation of $\partial O / \partial m_i$

The partial derivative of our objective function with respect to the ith movement parameter can be expressed as

$$\frac{\partial O}{\partial m_i} = \overbrace{2(\mathbf{f}_+ - \mathbf{f}_-)^T}^{\text{outer derivative}}_{1 \times n} \overbrace{\frac{\partial \mathbf{f}_+}{\partial m_i}}^{\text{inner derivative}}_{n \times 1} \qquad [\text{B3}]$$

where the derivatives of the image w.r.t. the movement parameters are expressed in mm^{-1} and radians^{-1}, and

where its jth element of $\mathbf{x}' = \mathbf{T}(\mathbf{m})\mathbf{x} + d(\mathbf{x}, \mathbf{c})\mathbf{v}$ is calculated according to

$$\left(\frac{\partial \mathbf{f}_+}{\partial m_i}\right)_j = \frac{1}{\delta} \langle ((\mathbf{M}^{-1}\mathbf{W}_i\mathbf{M})\mathbf{x}_j' - \mathbf{x}_j'), \nabla \mathbf{f}_+|_{\mathbf{x}_{j'}} \rangle \qquad [\text{B4}]$$

$\mathbf{M}$ in Eq. [B4] is

$$\mathbf{M} = \begin{bmatrix} s_x & 0 & 0 & x_{off} \\ 0 & s_y & 0 & y_{off} \\ 0 & 0 & s_z & z_{off} \\ 0 & 0 & 0 & 1 \end{bmatrix} \qquad [\text{B5}]$$

and represents the mapping from voxel to metric coordinates. s_x, s_y, s_z defines the voxel size, and x_{off}, y_{off}, z_{off} is the translation between the origin of the voxel system and the rotation point. $\mathbf{W}_i$ reflects how a δ change of motion parameter i changes the metric coordinate frame

$$\mathbf{W}_1 = \begin{bmatrix} 1 & 0 & 0 & \delta \\ 0 & 1 & 0 & 0 \\ 0 & 0 & 1 & 0 \\ 0 & 0 & 0 & 1 \end{bmatrix}, \quad \mathbf{W}_2 = \begin{bmatrix} 1 & 0 & 0 & 1 \\ 0 & 1 & 0 & \delta \\ 0 & 0 & 1 & 0 \\ 0 & 0 & 0 & 1 \end{bmatrix}, \quad \mathbf{W}_3 = \begin{bmatrix} 1 & 0 & 0 & 1 \\ 0 & 1 & 0 & 0 \\ 0 & 0 & 1 & \delta \\ 0 & 0 & 0 & 1 \end{bmatrix}, \quad \mathbf{W}_4 = \begin{bmatrix} 1 & 0 & 0 & 0 \\ 0 & \cos(\delta) & \sin(\delta) & 0 \\ 0 & -\sin(\delta) & \cos(\delta) & 0 \\ 0 & 0 & 0 & 1 \end{bmatrix}$$

$$\mathbf{W}_5 = \begin{bmatrix} \cos(\delta) & 0 & \sin(\delta) & 0 \\ 0 & 1 & 0 & 0 \\ -\sin(\delta) & 0 & \cos(\delta) & 0 \\ 0 & 0 & 0 & 1 \end{bmatrix}, \quad \mathbf{W}_6 = \begin{bmatrix} \cos(\delta) & \sin(\delta) & 0 & 0 \\ -\sin(\delta) & \cos(\delta) & 0 & 0 \\ 0 & 0 & 1 & 0 \\ 0 & 0 & 0 & 1 \end{bmatrix}$$

The derivation of $\partial/O/\partial c_i$ is

$$\frac{\partial O}{\partial c_i} = \overbrace{2(\mathbf{f}_+ - \mathbf{f}_-)^T}^{\text{outer derivative}}_{1 \times n} \overbrace{\left(\frac{\partial \mathbf{f}_+}{\partial c_i} - \frac{\partial \mathbf{f}_-}{\partial c_i}\right)}^{\text{inner derivative}}_{n \times 1} \qquad [\text{B6}]$$

The outer derivative of [B6] is the same as above. The inner derivatives of Eq. [B6] w.r.t. c_i become

$$\begin{cases} \dfrac{\partial \mathbf{f}_+}{\partial c_i} = \dfrac{\partial}{\partial c_i}(\mathbf{I}_+ \odot \mathbf{J}_+) = \dfrac{\partial \mathbf{I}_+}{\partial c_i} \odot \mathbf{J}_+ + \mathbf{I}_+ \odot \dfrac{\partial \mathbf{J}_+}{\partial c_i} \\ \dfrac{\partial \mathbf{f}_-}{\partial c_i} = \dfrac{\partial}{\partial c_i}(\mathbf{I}_- \odot \mathbf{J}_-) = \dfrac{\partial \mathbf{I}_-}{\partial c_i} \odot \mathbf{J}_- + \mathbf{I}_- \odot \dfrac{\partial \mathbf{J}_-}{\partial c_i} \end{cases} \quad [\text{B7}]$$

The $\mathbf{I}_+$ and $\mathbf{I}_-$ images are functions of $d(\mathbf{c})$, which in turn is a function of $\mathbf{c}$. According to the chain rule, the derivatives of $\mathbf{I}_+$ and $\mathbf{I}_-$ w.r.t. c_i are

$$\frac{\partial \mathbf{I}_+}{\partial c_i} = \frac{\partial}{\partial d}[\mathbf{I}_+] \odot \frac{\partial}{\partial c_i} d(\mathbf{c}) \qquad [\text{B8}]$$

$$\frac{\partial z \mathbf{I}_-}{\partial c_i} = \frac{\partial}{\partial d}[\mathbf{I}_-] \odot \frac{\partial}{\partial c_i} d(\mathbf{c}) \qquad [\text{B9}]$$

The first factor in Eq. [B8] is calculated as

$$\frac{\partial}{\partial d}[\mathbf{I}_+] = \frac{I_+(\mathbf{x}' + \Delta d\mathbf{v}) - I_+(\mathbf{x}')}{\Delta d} = \langle \nabla I_+, \mathbf{v} \rangle = D_\mathbf{v}(I_+)$$

$$[\text{B10}]$$

which is the directional derivative of $\mathbf{I}_+$ along $\mathbf{v}$. Correspondingly, the first factor in Eq. [B9] is the directional derivative of $\mathbf{I}_-$ along $-\mathbf{v}$

$$\frac{\partial}{\partial d}[\mathbf{I}_-] = \langle \nabla I_-, -\mathbf{v} \rangle = -\langle \nabla I_-, \mathbf{v} \rangle = -D_\mathbf{v}(I_-) \quad [\text{B11}]$$

The second factor of Eqs. [B8] and [B9] is the same, and is the inner derivative of $\mathbf{I}_+$ and $\mathbf{I}_-$

$$\frac{\partial}{\partial c_i} d(\mathbf{c}) = \frac{\partial}{\partial c_i} \sum_{k=1}^{N} c_k \boldsymbol{\beta}_3 = \begin{bmatrix} \text{all terms but } i = k \\ \text{become zero} \end{bmatrix} = \boldsymbol{\beta}_{3,i}$$

$$[\text{B12}]$$

which simply is the unscaled ith B-spline, shifted in the image volume depending on the index $i = (k_z N_{c,y} + k_y) N_{c,x} + k_x$, where $N_{c,x} N_{c,y}$ denote the number of coefficients in the x and y direction, respectively. Equations [B8] and [B9] become

$$\begin{cases} \dfrac{\partial \mathbf{I}_+}{\partial c_i} = D_\mathbf{v}(\mathbf{I}_+)\boldsymbol{\beta}_{3,i} \\ \dfrac{\partial \mathbf{I}_-}{\partial c_i} = -D_\mathbf{v}(\mathbf{I}_-)\boldsymbol{\beta}_{3,i} \end{cases} \qquad [\text{B13}]$$

The second terms of Eqs. [B7] contain the derivatives of the Jacobian w.r.t. the coefficient c_i.

$$
\begin{cases}
\dfrac{\partial \mathbf{J}_+}{\partial c_i} = \dfrac{\partial}{\partial c_i}\left[1 + \left(\sum_{k=1}^{N} c_k D_{\mathbf{v}}(\boldsymbol{\beta}_3) \right) \right] = \left[\begin{array}{c} \text{all terms but } i=k \\ \text{become zero} \end{array} \right| \quad = D_{\mathbf{v}}(\boldsymbol{\beta}_{3,i}) \\[2em]
\dfrac{\partial \mathbf{J}_-}{\partial c_i} = \dfrac{\partial}{\partial c_i}\left[1 - \left(\sum_{k=1}^{N} c_k D_{\mathbf{v}}(\boldsymbol{\beta}_3) \right) \right] \qquad\qquad\qquad\quad = -D_{\mathbf{v}}(\boldsymbol{\beta}_{3,i})
\end{cases}
$$

[B14]

Since Eqs. [B13] and [B14] are zero outside the support of the ith B-spline, so are Eqs. [B7] and [B6], which allows for reasonable computation times for the entire vector of partial derivatives of the objective function.

In summary, using Eqs. [B7]–[B14], the final expression in Eq. [B6] becomes

$$
\begin{aligned}
\frac{\partial O}{\partial c_i} &= \overbrace{2(\mathbf{f}_+ - \mathbf{f}_-)^T}^{\text{outer derivative}}\underbrace{\overbrace{\left(\left(\frac{\partial \mathbf{I}_+}{\partial c_i} \odot \mathbf{J}_+ + \mathbf{I}_+ \odot \frac{\partial \mathbf{J}_+}{\partial c_i} \right) - \left(\frac{\partial \mathbf{I}_-}{\partial c_i} \odot \mathbf{J}_- + \mathbf{I}_- \odot \frac{\partial \mathbf{J}_-}{\partial c_i} \right) \right)}^{\text{inner derivative}}}_{n \times 1} \\
&= 2(\mathbf{f}_+ - \mathbf{f}_-)^T \left(\begin{array}{c} (D_{\mathbf{v}}(\mathbf{I}_+) \odot \boldsymbol{\beta}_3 \odot \mathbf{J}_+ + \mathbf{I}_+ \odot D_{\mathbf{v}}(\boldsymbol{\beta}_3)) - \cdots \\ (-D_{\mathbf{v}}(\mathbf{I}_-) \odot \boldsymbol{\beta}_3 \odot \mathbf{J}_- + \mathbf{I}_- \odot -D_{\mathbf{v}}(\boldsymbol{\beta}_3)) \end{array} \right) \\
&= 2(\mathbf{f}_+ - \mathbf{f}_-)^T \left(\begin{array}{c} \{D_{\mathbf{v}}(\mathbf{I}_+) \odot \mathbf{J}_+ + D_{\mathbf{v}}(\mathbf{I}_-) \odot \mathbf{J}_-\} \odot \boldsymbol{\beta}_3 + \cdots \\ \{\mathbf{I}_+ + \mathbf{I}_-\} \odot D_{\mathbf{v}}(\boldsymbol{\beta}_3) \end{array} \right)
\end{aligned}
$$

[B15]

where $1 \times n$ labels the $2(\mathbf{f}_+ - \mathbf{f}_-)^T$ term.

The "i" in $\beta_{3,i}$ was dropped to indicate that the same β_3 is used for all i.

ACKNOWLEDGMENTS

REFERENCES

1. Bartels LW, Smits HF, Bakker CJ, Viergever MA. MR imaging of vascular stents: effects of susceptibility, flow, and radiofrequency eddy currents. J Vasc Interv Radiol 2001;12:365–371.
2. Shellock FG. MR imaging of metallic implants and materials: a compilation of the literature. AJR Am J Roentgenol 1988;151:811–814.
3. Shellock FG, Curtis JS. MR imaging and biomedical implants, materials, and devices: an updated review. Radiology 1991;180:541–550.
4. Shellock FG, Morisoli S, Kanal E. MR procedures and biomedical implants, materials, and devices: 1993 update. Radiology 1993;189:587–599.
5. Miller JB, Garroway AN. Removal of static-field inhomogeneity and chemical-shift effects in NMR imaging. J Magn Reson 1986;67:575–579.
6. Kim JK, Plewes DB, Henkelman RM. Phase constrained encoding (PACE): a technique for MRI in large static field inhomogeneities. Magn Reson Med 1995;33:497–505.
7. McIntyre DJ, Hennel F, Morris PG. SPARE: a robust method for magnetic resonance imaging in inhomogeneous fields. J Magn Reson 1998;130:58–62.
8. Glover GH, Schneider E. 3-Point Dixon technique for true water fat decomposition with B_o inhomogeneity correction. Magn Reson Med 1991;18:371–383.
9. Sekihara K, Matsui S, Kohno H. NMR imaging for magnets with large nonuniformities. IEEE Trans Med Imaging 1985;MI-4:193–199.
10. Sumanaweera TS, Glover GH, Hemler PF, van den Elsen PA, Martin D, Adler JR, Napel S. MR geometric distortion correction for improved frame-based stereotaxic target localization accuracy. Magn Reson Med 1995;34:106–113.
11. Jezzard P, Balaban RS. Correction for geometric distortion in echo planar images from B0 field variations. Magn Reson Med 1995;34:65–73.
12. Chavez S, Xiang QS, An L. Understanding phase maps in MRI: a new cutline phase unwrapping method. IEEE Trans Med Imaging 2002;21:966–977.
13. Cusack R, Papadakis N. New robust 3-D phase unwrapping algorithms: application to magnetic field mapping and undistorting echoplanar images. Neuroimage 2002;16(3 Pt 1):754–764.
14. Hedley M, Rosenfeld D. A new two-dimensional phase unwrapping algorithm for MRI images. Magn Reson Med 1992;24:177–181.
15. Jenkinson M. Fast, automated, N-dimensional phase-unwrapping algorithm. Magn Reson Med 2003;49:193–197.
16. Szumowski J, Coshow WR, Li F, Quinn SF. Phase unwrapping in the three-point Dixon method for fat suppression MR imaging. Radiology 1994;192:555–561.
17. Chen NK, Wyrwicz AM. Correction for EPI distortions using multi-echo gradient-echo imaging. Magn Reson Med 1999;41:1206–1213.
18. Butts K, Pauly JM, Daniel BL, Kee S, Norbash AM. Management of biopsy needle artifacts: techniques for RF-refocused MRI. J Magn Reson Imaging 1999;9:586–595.
19. Cho ZH, Kim DJ, Kim YK. Total inhomogeneity correction including chemical shifts and susceptibility by view angle tilting. Med Phys 1988;15:7–11.
20. Chang H, Fitzpatrick JM. A technique for accurate magnetic-resonance-imaging in the presence of field inhomogeneities. IEEE Trans Med Imaging 1992;11:319–329.
21. Kannengiesser SA, Wang Y, Haacke EM. Geometric distortion correction in gradient-echo imaging by use of dynamic time warping. Magn Reson Med 1999;42:585–590.

22. Morgan PS, Bowtell RW, McIntyre DJ, Worthington BS. Correction of spatial distortion in EPI due to inhomogeneous static magnetic fields using the reversed gradient method. J Magn Reson Imaging 2004;19: 499–507.

23. Andersson JL, Skare S, Ashburner J. How to correct susceptibility distortions in spin-echo echo-planar images: application to diffusion tensor imaging. Neuroimage 2003;20:870–888.

24. Marsden JE, Tromba AJ. Vector calculus. San Francisco: Freeman; 1981.

25. Bowtell R, McIntyre DJO, Commandre M-J, Glover PM, Mansfield P. Correction of geometric distortion in echo planar images. In: Proceedings of the 2nd Annual Meeting of ISMRM, San Francisco, 1994. p 411.

26. Ashburner J, Friston KJ. Nonlinear spatial normalization using basis functions. Hum Brain Mapp 1999;7:254–266.

27. deBoor C. A practical guide to splines. New York: Springer-Verlag; 1978.

28. Hou HS, Andrews HC. Cubic splines for image interpolation and digital filtering. IEEE Trans Acoust Speech Signal Processing 1978;ASSP-26: 508–517.

29. Schoenberg IJ. Contribution to the problem of approximation of equidistant data by analytic functions. Q Appl Math 1946;4:45–99,112–141.

30. Kybic J, Thevenaz P, Nirkko A, Unser M. Unwarping of unidirectionally distorted EPI images. IEEE Trans Med Imaging 2000;19:80–93.

31. Kybic J, Unser M. Fast parametric elastic image registration. IEEE Trans Image Processing 2003;12:1427–1442.

32. Unser M, Aldroubi A, Eden M. Fast B-spline transforms for continuous image representation and interpolation. IEEE Trans Pattern Anal Machine Intel 1991;13:277–285.

33. Thevenaz P, Ruttimann UE, Unser M. A pyramid approach to subpixel registration based on intensity. IEEE Trans Image Processing 1998;7: 27–41.

34. Unser M, Aldroubi A, Eden M. B-spline signal-processing. I. Theory. IEEE Trans Signal Processing 1993;41:821–833.